Desalination 528 (2022) 115606

Contents lists available at ScienceDirect

Desalination

journal homepage: www.elsevier.com/locate/desal

Utilizing Buckingham Pi theorem and multiple regression analysis in scaling up direct contact membrane distillation processes

Heba Khafajah [a,b], Mohamed I. Hassan Ali [a,b,d,*,1], Navya Thomas [b,c], Isam Janajreh [a,b], Hassan A. Arafat [b,e]

[a] Department of Mechanical Engineering, Khalifa University, Abu Dhabi, United Arab Emirates
[b] Center for Membrane and Advanced Water Technology, Khalifa University, Abu Dhabi, United Arab Emirates
[c] Cranfield Water Science Institute, Cranfield University, Bedfordshire MK43 0AL, UK
[d] Mechanical Power Engineering Department, Helwan University, Cairo, Egypt
[e] Department of Chemical Engineering, Khalifa University, Abu Dhabi, United Arab Emirates

HIGHLIGHTS

- Buckingham Pi-theorem used to model DCMD performance with dimensionless parameters.
- DCMD process performance represented by eight dimensionless groups
- Reliability of predicted relationships confirmed with experimental and CFD data.
- Generated correlations predicted MD performance for small and large-scale modules.
- Proposed approach can be extended to other MD configurations.

ARTICLE INFO

Keywords:
DCMD
Dimensional analysis
Pi theorem
Scale up
Regression analysis

ABSTRACT

Predicting the performance of a full-scale direct contact membrane distillation (DCMD) module based on experimental lab-scale results is rather difficult, since the DCMD performance is dependent on many different process parameters. Hence, there is a need for a methodology to perform DCMD system up-scaling based on lab-scale experimental results. In this study, we devise an approach to scale up the performance of DCMD systems by using the Buckingham's Pi theorem to group the DCMD process parameters into eight relevant dimensionless groups. Experimental data obtained from literature at various module dimensions were used to evaluate the developed dimensionless groups. An experimentally validated computational fluid dynamics (CFD) model was also developed and used to extend the coverage of operational parameters beyond the available experimental data. Then, two empirical dimensionless correlations were created, using multiple nonlinear regression analysis, and then validated, to enable the prediction of flux and pressure drop in DCMD systems at any scale.

1. Introduction

Seawater desalination is growing globally to address water scarcity issues attributed to rapid urbanization, population growth, and climate change [1]. Membrane distillation (MD), a third generation desalination technology, can help in this regard by treating hypersaline feed solutions from different sources, including the brine from desalination plants [2]. This non-isothermal process benefits from low operating temperature and pressure, making it compatible with solar and geothermal energy, or even waste heat [3], while lowering its capital and maintenance costs [4]. MD uses a partial vapor pressure differential caused by a temperature gradient across a hydrophobic porous membrane to induce separation and is dominantly operated in one of three configurations: direct contact MD (DCMD), air gap MD (AGMD), and vacuum MD (VMD) [5].

It has been reported that there is a significant difference between lab and full-scales MD process performance [6]. While many lab-scale studies have thoroughly studied the impacts of various operational parameters on the performance of MD (e.g., [7–11]), only few have

* Corresponding author at: Department of Mechanical Engineering, Khalifa University, Abu Dhabi, United Arab Emirates.
E-mail address: mohamed.ali@ku.ac.ae (M.I. Hassan Ali).
[1] (on leave)

https://doi.org/10.1016/j.desal.2022.115606
Received 1 December 2021; Received in revised form 7 January 2022; Accepted 24 January 2022
Available online 5 February 2022

actually attempted to utilize lab-scale results in modeling full-scale MD systems. Notable examples of the latter group include the work of Gustavson et al. [12] and Zhang et al. [13], who developed step-wise models, which were tested against lab-scale flat-sheet modules in an attempt to replicate them in full-scale conditions. Sirkar et al. [14] applied a similar modeling approach to hollow fiber modules. Winter [15] presented a large collection of full-scale models that are solved step-wise and validated against SolarSpring®'s commercial modules. Hitsov et al. [16] calibrated model equations using lab scale data, using Monti Carlo filtering method, then applied them to a full-scale module, considering the compaction effect at full-scale [17]. Dong developed two open-source simulators for flat sheet and hollow fiber membranes using the Matlab GUI platform, to complement DCMD module scale up. Based on lab-scale results in both configurations, the developed simulators were able to predict large-scale DCMD module performance in both counter-current and co-current operation [18]. Despite the fact that their process for scaling up the DCMD was successful, their models are heavily reliant on the outcomes of lab calibrations.

The usability of data from lab-scale studies is limited by a lack of a uniform system up-scaling technique, as well as by the inadequate details provided on key process parameters in the said studies (e.g., flow channel dimensions, pressure drop in feed channel, membrane type, etc.). Thus, there is a dire need to develop a standard MD performance analysis and up-scaling tool. This can be achieved using dimensional analysis. Dimensional analysis, which provides a relation between dependent and independent variables, is a useful and established tool for scale-up in process industry [19–22]. Dimensional analysis can be performed using the Buckingham Pi-theorem by identifying a number of dimensionless terms that well describe the phenomenon on hand. Its utility stems from its ability to estimate full-scale system performance using data collected on a lab-scale, thus reducing the cost and time needed for estimating the requirements for system scaling purposes. Very recently, Najib et al. [23] applied the Pi-theorem for the first time to model multiple effect VMD and established correlations between these dimensionless terms to predict the recovery ratio and gained output ratio of the system.

In this study, we established a standardized protocol for scaling up MD processes using Pi-theorem, taking DCMD as an example. The ultimate goal was to enable the prediction of full-scale MD process' permeate flux and feed pressure drop, using a small number of representative dimensionless groups as input terms. These dimensionless groups were first formulated using Buckingham Pi theorem and validated using data from three published experimental studies. Then, using multiple nonlinear regression analysis, the inter-correlations between these groups, which combine the most influential process parameters (feed flow rate, feed and permeate temperatures, feed channel dimensions, and feed properties), were consolidated into one equation to predict the permeate flux and pressure drop in a full-scale DCMD system.

2. Theory

2.1. Transport phenomena in DCMD

In MD, heat and mass transfer occur simultaneously across a hydrophobic membrane thanks to water vapor pressure difference between the feed and permeate sides of the membrane. The temperature difference between the membrane/feed and membrane/permeate interfaces creates this pressure difference, generating a vapor flux. In DCMD, the transferred water vapor condensates in the permeate stream, releasing both latent and sensible heat [24]. As depicted in Fig. S1 (supplementary information, SI), heat transfer in DCMD occurs in three stages: (i) from the bulk of hot feed solution to the membrane surface on the feed side, through the feed side thermal boundary layer, (ii) via evaporation and vapor transport through the membrane's pores and via conduction across the solid membrane matrix and pore gases, and (iii) from the membrane's surface on the permeate side to the cold permeate bulk solution, through the permeate boundary layer. The vapor flux (kg/m^2 s) in MD is calculated from [25].

$$J = B_m \cdot \left(P_{m,f} - P_{m,p}\right) \tag{1}$$

where B_m is the membrane distillation coefficient (kg/m^2 Pa s), $P_{m,\,f}$ and $P_{m,\,p}$ are the water vapor pressure (Pa) on the membrane's feed and permeate side, respectively. The vapor pressures depend on the bulk feed and permeate temperature (T_f and T_p, respectively), and can be calculated from Antoine equation [26]:

$$P_{m,i} = exp\left(23.1964 - \frac{3816.44}{T_i(K) - 46.13}\right) \tag{2}$$

where T_i is temperature (K). The temperature polarization coefficient (TPC) provides an indication of the effect of boundary layers on heat transfer in MD. It is expressed as:

$$TPC = \frac{T_{mf} - T_{mp}}{T_f - T_p} \tag{3}$$

where T_{mf} and T_{mp} are the membrane surface temperatures at the feed and permeate side, respectively. The convective heat transfer rate per unit area (W/m^2) on the feed and permeate sides can be calculated using Eqs. (4) and (5), respectively:

$$\dot{q}_f = h_f\left(T_f - T_{f,m}\right) \tag{4}$$

$$\dot{q}_p = h_p\left(T_p - T_{p,m}\right) \tag{5}$$

where subscripts *f, p, and m* refer to feed, permeate, and membrane, respectively, and h is the convective heat transfer coefficient (W/m^{2}K). The overall rate of heat transfer per unit area (W/m^2) across the membrane is calculated as:

$$\dot{q}_m = \dot{q}_{vap} + \dot{q}_{cond} = J.h_{fg} + \frac{k_m}{\delta_m}\left(T_{f,m} - T_{p,m}\right) \tag{6}$$

where J is permeate flux (kg/m^2 s), h_{fg} is the latent heat of vaporization (J/kg), k_m is the effective membrane conductivity (W/mK), and δ_m is the membrane thickness (m). The thermal conductivity of the membrane can be calculated as [27]:

$$k_m = (1 - \varepsilon)k_s + \varepsilon k_g \tag{7}$$

where ε is the membrane porosity, k_s and k_g are the thermal conductivities of the membrane material and the gas in the membrane pores, respectively. Under steady-state condition, $\dot{q}_f, \dot{q}_p$, and $\dot{q}_m$ are equal.

2.2. Buckingham's Pi theorem and its application to DCMD

The Buckingham Pi-theorem states that if n dimensional parameters, $q_1, q_2, q_3 \ldots q_n$, are physically related to a given system/phenomenon and are interrelated by an unknown set of equations, then these parameters can be expressed via a functional relationship of the form: $f(q_1, q_2, \ldots q_n) = 0$. Also, if m is the number of basic dimensions required to represent the units of the n parameters (in MD, the relevant basic dimensions are length (L), mass (M), time (T), and temperature (θ), termed LMTθ), then, a maximum of *n-m* independent dimensionless groups can be created for this system. If we call these dimensionless groups $\pi_1, \pi_2, \ldots \pi_{n-m}$, then the functional relationship can be reduced to the dimensionless form: $\pi_1 = f(\pi_2, \pi_3, \ldots \pi_{n-m})$.

Thus, in this work, the first step in formulating the dimensionless groups for DCMD was to identify the operational parameters that affect the DCMD process. As 24 such parameters were initially identified, we made the following assumptions to reduce the number of parameters included:

Table 1
Operational parameters associated with momentum, heat, and mass transfer in DCMD, their units and base (LMTθ) units.

Parameters	Symbol	SI Unit	LMTθ base unit
Momentum transfer-related parameters			
Permeate flux	J	kg·m^{-2}·s^{-1}	M·L^{-2}·T^{-1}
Pressure drop in feed channel	Δp	kg·m^{-1}·s^{-2}	M·T^{-2}·L^{-1}
Feed channel length	L	m	L
Feed channel hydraulic diameter	D_h	m	L
Feed dynamic viscosity	μ	kg·m^{-1}·s^{-1}	M·L^{-1}·T^{-1}
Feed density	ρ	kg·m^{-3}	M.L^{-3}
Free velocity	u_f	ms^{-1}	L·T^{-1}
Heat transfer-related parameters			
Parameters	Symbol	SI Unit	LMTθ base unit
Feed thermal conductivity	k_f	kg·m·K^{-1}·s^{-3}	M·L·θ^{-1}·T^{-3}
Feed density	ρ	kg·m^{-3}	M·L^{-3}
Feed dynamic viscosity	μ	kg·m^{-1}·s^{-1}	M.L^{-1}·T^{-1}
Feed specific heat capacity	c_p	m^{2}K^{-1}·s^{-2}	L.^{2}θ^{-1}·T^{-2}
Feed side convective heat transfer coefficient	h_f	kg·K^{-1}·s^{-3}	M.θ^{-1}·T^{-3}
Feed channel hydraulic diameter	D_h	m	L
Mass transfer-related parameters			
Parameters	Symbol	SI Unit	LMTθ base unit
Mass diffusivity of water on the feed side	D_{mass}	m^2·s^{-1}	L^2·T^{-1}
Mass transfer coefficient of water on the feed side	k_{mass}	m·s^{-1}	L·T^{-1}
Feed density	ρ	kg·m^{-3}	M·L^{-3}
Feed dynamic viscosity	μ	kg·m^{-1}·s^{-1}	M·L^{-1}·T^{-1}
Feed channel hydraulic diameter	D_h	m	L

1. As the feed side parameters are more crucial for the performance of DCMD system only the feed side parameters are considered for the modeling purpose [24].
2. The system was assumed to be thermally well-insulated and thus the heat loss to the surrounding environment was ignored.
3. The feed and permeate flow channels were assumed to have the same channel dimensions and devoid of spacers. The feed and permeate flows were considered to operate at similar velocities.
4. Any parameters that were expected to remain unchanged upon scaling-up from lab-scale to full-scale were not considered. This mainly includes the parameters related to the membrane itself (e.g., membrane thickness, tortuosity, pores size, contact angle (CA), etc.), which can be assumed to remain the same between the lab-scale and full-scale systems. It also includes the temperature of the feed and permeate inlet streams (note: the ratio of these temperatures was considered, however).
5. The effects of membrane compaction, membrane wetting, and fouling were neglected.

This resulted in the selected parameters shown in Table 1, which were categorized based on their relevance to momentum, mass, or heat transfer in DCMD. Also shown in Table 1 are the SI and basic units (LMTθ) of the parameters. Consequently, the functional relationships depicted in Eqs. (8), (9), and 10, were established for momentum, heat, and mass transfer, respectively:

$$f\left(J, \Delta p, u_f, \rho, \mu, L, D_h\right) = 0 \tag{8}$$

$$f\left(h_f, c_p, k_f, \mu, D_h, \rho\right) = 0 \tag{9}$$

$$f(k_{mass}, \mu, D_{mass}, \rho, D_h) = 0 \tag{10}$$

For the momentum transport group, which includes seven parameters with 3 base units (LMT, see Table 1), four dimensionless groups (7–3 = 4) can be generated as follows:

Table 2
Dimensionless numbers resulting from the application of Buckingham's Pi-theorem to the three transport phenomena in DCMD.

Groups	Dimensionless number	Symbol	Name	Definition
Dimensionless numbers associated with momentum transfer				
$\pi_1 = f(J, u_f, D_h, \rho)$	$\pi_1 = \frac{J}{u_f \rho}$	FF	Flux Factor	Ratio of permeate flux through the membrane to feed flow rate.
$\pi_2 = f(\Delta p, u_f, D_h, \rho)$	$\pi_2 = \frac{\Delta p}{{u_f}^2 \rho}$	*Eu*	Euler Number	Ratio of pressure force to inertia force.
$\pi_3 = f(\mu, u_f, D_h, \rho)$	$\pi_3 = \frac{\mu}{D_h\, u_f \rho}$	*Re*[*]	Reynolds Number	Ratio of inertia force to viscous force.
$\pi_4 = f(L, u_f, D_h, \rho)$	$\pi_4 = \frac{L}{D_h}$	GF	Geometry Factor	Ratio of channel length to its hydraulic diameter.
Dimensionless numbers associated with heat transfer				
Groups	Dimensionless Number	Symbol	Name	Definition
$\pi_5 = f(h_f, k_f, \rho, \mu, D_h)$	$\pi_5 = \frac{h_f D_h}{k_f}$	*Nu*	Nusselt Number	Ratio of convective heat transfer to conductive heat transfer.
$\pi_6 = f(c_p, k_f, \rho, \mu, D_h)$	$\pi_6 = \frac{\mu\, c_p}{k_f}$	*Pr*	Prandtl Number	Ratio of thermal diffusion to viscous diffusion.
Dimensionless numbers associated with mass transfer				
Groups	Dimensionless Number	Symbol	Name	Definition
$\pi_7 = f(h_{mass}, D_{mass}, \rho, D_h)$	$\pi_7 = \frac{h_{mass} D_h}{D_{mass}}$	*Sh*	Sherwood Number	Ratio of convective mass transfer to diffusive mass transfer.
$\pi_8 = f(\mu, D_{mass}, \rho, D_h)$	$\pi_8 = \frac{\mu}{\rho\, D_{mass}}$	*Sc*	Schmidt Number	Ratio of momentum diffusivity (kinematic viscosity) to mass diffusivity.

[*] Note: Due to its dimensionless nature, $1/Re$ was later substituted with *Re* in the regression analysis, along with the needed coefficient adjustment.

$$\pi_1 = f\left(J, u_f, D_h, \rho\right) \tag{11}$$

$$\pi_2 = f\left(\Delta p, u_f, D_h, \rho\right) \tag{12}$$

$$\pi_3 = f\left(\mu, u_f, D_h, \rho\right) \tag{13}$$

$$\pi_4 = f\left(L, u_f, D_h, \rho\right) \tag{14}$$

These dimensionless groups were determined as described in the SI.

The first dimensionless group is: $\pi_1 = \frac{J}{u_f \rho}$, to be henceforth denoted the *flux factor* (FF). FF represents the ratio of permeate flux through the membrane to the flow rate through the feed channel. Besides, the second dimensionless group is: $\pi_2 = \frac{\Delta p}{{u_f}^2 \rho}$, which is the ratio between pressure force to inertia force and is already known in literature as Euler's number (*Eu*). Applying the same procedure again leads to $\pi_3 = \frac{\mu}{D_h\, u_f \rho}$, which is the inverse of the well-known Reynolds number (*Re*) (*Re*: ratio between inertial to viscous forces). Due to its dimensionless nature, $1/\pi_3$ was later substituted with *Re* in the regression analysis, along with the needed coefficient adjustment. Starting with Eq. ((14), the fourth dimensionless number was determined to be $\pi_4 = \frac{L}{D_h}$, which is referred to as the *geometry factor* (GF), which represents the ratio of the flow channel length to its hydraulic diameter.

The same procedure was followed for the determination of the dimensionless numbers associated with heat transfer. With 6 parameters and 4 base units (LMTθ) (Table 1), 2 dimensionless groups (6–4 = 2) were determined for heat transfer, starting with the following equations:

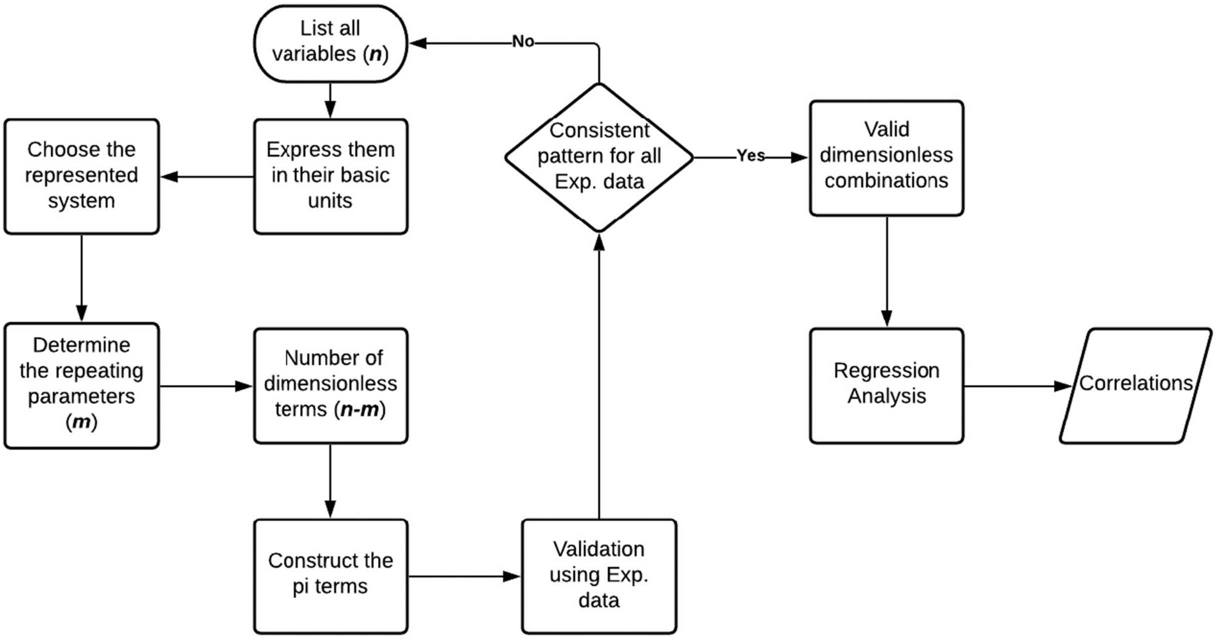

Fig. 1. Flowchart depicting the procedure followed to establish the empirical relationships describing the DCMD system based on Buckingham Pi theorem and regression analysis.

$$\pi_5 = f\left(h_f, k_f, \rho, \mu, D_h\right) \quad (15)$$

$$\pi_6 = f\left(c_p, k_f, \rho, \mu, D_h\right) \quad (16)$$

Following the above procedure, the resultant dimensionless groups were $\pi_5 = \frac{h_f D_h}{k_f}$ and $\pi_6 = \frac{\mu\, c_p}{k_f}$, which are already known as the Nusselt (*Nu*) and Prandtl's (*Pr*) numbers, respectively. Lastly, for mass transfer related groups, 5 parameters and 3 base units (LMT) (Table 1) yielded 2 dimensionless groups (5–3 = 2), which were determined starting with the following equations:

$$\pi_7 = f\left(k_{mass}, D_{mass}, \rho, D_h\right) \quad (17)$$

$$\pi_8 = f\left(\mu, D_{mass}, \rho, D_h\right) \quad (18)$$

This resulted in $\pi_7 = \frac{h_{mass} D_h}{D_{mass}}$ and $\pi_8 = \frac{\mu}{\rho\, D_{mass}}$, which are known as Sherwood (*Sh*) and Schmidt (*Sc*) numbers, respectively. Table 2 summarizes all eight dimensionless groups of the DCMD system.

3. Methodology

A flowchart depicting the general methodology followed in this work to formulate the empirical relationships describing the DCMD system based on Buckingham Pi theorem is depicted in Fig. 1, which is based on the protocol detailed in [28] for dimensional analysis. The methodology includes the following main steps in order:

1. Formulation of the dimensionless groups of relevance that can adequately describe the system, as detailed in Section 2.2.
2. Studying the trends and inter-dependencies of the obtained dimensionless groups using data from three well-described experimental studies from literature, as a means of validating the significance of these dimensionless groups vis-à-vis the DCMD system.
3. Using computational fluid dynamics (CFD) modeling, generation of DCMD performance data (mainly, flux and pressure drop) covering a much wider range of dimensionless groups values than what is readily available in open literature.
4. Using nonlinear regression analysis, generation of non-dimensional empirical correlations for the prediction of flux and pressure drop in DCMD systems of any scale and verifying the validity of these correlations using CFD data.

3.1. CFD modeling and validation

A major challenge we faced in this work is finding literature experimental DCMD studies that i) cover a wide range of operational parameters (including both laminar and turbulent feed flow) and system performance results (including pressure drop in the field channel), to enable covering a wide value range of dimensionless numbers values, AND ii) reported thoroughly the design specifications of the DCMD system used (including flow channel length, depth, and width, flow velocity, density, and viscosity, etc.). Since such studies with thorough, wide-range data reporting were rare, we resorted to CFD modeling to generate system performance results for a wide range of input parameters. Star-CCM+ (double precision Star-CCM + 12.06.010-R8, Siemens Product Lifecycle Management Software Inc., Plano, Texas) was used as a platform for the CFD model development and simulations. The models operated under steady state condition for laminar and turbulent flow regimes in all CFD simulations. Following are the methodology details of the CFD modeling.

3.2. Governing equations

The permeate flux *J* was calculated by conducting surface integration of the local flux values, *J(y,z)*, as follows:

$$J = \frac{B_m}{A}\left[\iint P^{vap}_{m,f}(y,z)\, dy\, dz - \iint P^{vap}_{m,p}(y,z)\, dy\, dz\right] \quad (19)$$

where B_m was assumed to be independent of the other operational parameters, as suggested by [12]. A flat sheet (FS) DCMD module was assumed to have an active membrane area A, while y and z indicate the location on the membrane surface. The permeate flux was linked to the mass, momentum, energy conservations equations (Eqs. (20), (21), and (22), respectively) as source terms. The mass, momentum, and energy source terms, S_j, S_m, and S_h, respectively, are shown in Eqs. (23-a), (23-b), (23-c) [24].

$$\nabla\cdot(\rho\vec{v}) = S_j \tag{20}$$

$$\nabla\cdot(\rho\vec{v}\vec{v}) = -\nabla P + \nabla\cdot(\vec{\tau}) + \rho\vec{g} + S_m \tag{21}$$

$$\nabla\cdot(\rho c_p T\vec{v}) = \nabla\cdot(k\nabla T) + S_h \tag{22}$$

$$S_j = \begin{cases} -\frac{J\cdot A}{V} \text{ at the feed} \Big/ \text{membrane interface} \\ \frac{J\cdot A}{V} \text{ at the permeate} \Big/ \text{membrane interface} \end{cases} \tag{23-a}$$

$$S_m = \begin{cases} -\frac{J\cdot A\cdot u}{V} \text{ at the feed} \Big/ \text{membrane interface} \\ \frac{J\cdot A\cdot u}{V} \text{ at the permeate} \Big/ \text{membrane interface} \end{cases} \tag{23-b}$$

$$S_h = \begin{cases} -\frac{\dot{q}_{vap}A}{V} \text{ at the feed} \Big/ \text{membrane interface} \\ \frac{\dot{q}_{vap}A}{V} \text{ at the permeate} \Big/ \text{membrane interface} \end{cases} \tag{23-c}$$

3.3. CFD geometry and boundary conditions

In the CFD simulations, as part of the modeled DCMD module, we included the feed channel, permeate channel, and the PTFE membrane. Error! Reference source not found. (SI) shows the direction of the applied feed inlet and the boundary conditions for the permeate outlet. A liquid domain was defined for the feed and permeate channels, while a solid volume was defined for the membrane. Boundaries for the inlets and outlets were set as velocity inlets and pressure outlets, respectively. The feed and permeate outlet boundaries were open to atmospheric pressure. The sidewall boundaries were considered as no-slip walls. A conjugated heat transfer boundary (feed/membrane and membrane/permeate) was selected for each internal interface boundary in Star-CCM+, which is known as a "contact interface thermal condition" [24]. The heat flux, as an energy source option, was specified at the interfaces. The feed/membrane interface source terms were set as leaving the feed channel, while the membrane/permeate gap source terms were set as entering the permeate channel. Then, the energy term was linked with the expression defined to calculate $\dot{q}_{vap}$. The mass and momentum source terms were similarly set and linked with an expression defined to calculate J across the membrane.

3.4. Mesh operation

In Star-CCM+, directed mesh operation was used to generate the three-dimensional mesh. Directed meshing is a method for generating high quality swept meshes in STAR-CCM+. The method sweeps a mesh from a surface towards a target surface, through its volume. A mesh independence analysis was performed to determine the appropriate mesh size and the required total number of mesh cells. To compare the mesh sensitivity results, the permeate flux was chosen as the response parameter for varying mesh size. The mesh size was refined by comparing permeate flux results in all three dimensions, and the permeate flux varied by less than 1% for the optimized mesh size.

3.5. Multiple nonlinear regression

Nonlinear regression involves a process of describing relationships between observations by means of multiple parameters and functions. The dependent parameters in a multiple nonlinear regression model are determined by several independent parameters through nonlinear combinations. The XLSTAT add-in tool in Excel® was used for developing two empirical correlations for membrane permeate flux and pressure drop in the feed channel as functions of process operating conditions, expressed in dimensionless form. XLSTAT is a highly intuitive and powerful tool, offering a user-friendly graphical interface by Visual Basic Application (VBA) and statistical calculation by C++. This program includes more than 100 statistical procedures for data analysis, regression, visualization, and forecasting. To create the empirical correlations using XLSTAT, values of the independent and dependent parameters were input in Excel and an equation form was initially assumed (e.g., linear, polynomial, exponential, etc.). The form was subsequently iteratively varied until an acceptable (i.e., > 0.9) coefficient of determination (R^2) was obtained. The assumption of homoscedasticity is internally applied by XLSTAT when fitting the relationship. R^2 (Eq. (24)) was utilized to determine the goodness of regression. In general, the closer the R^2 is to 1, the higher the accuracy.

Table 3
Values of process and membrane module parameters from Refs. [29–31].

Parameter	Ref. [29]	Ref. [30]	Ref. [31]
Geometry factor	201	62.5	20
Feed inlet temperature [°C]	60	60	60
Permeate inlet temperature [°C]	20	20	20
Feed/Permeate channel hydraulic diameter [mm][a]	1.99	1.6	5.8
Membrane type	PTFE	PTFE	PTFE
Membrane thickness [μm]	100	61	160
Membrane pore diameter [μm]	0.22	0.22	0.22
Feed/Permeate channel length [cm][a]	40	10	12
Feed/Permeate channel width [cm][a]	15	0.4	9.4
Feed/Permeate channel depth [mm][a]	1	1	3
Feed/Permeate inlet velocity [mm/s][a]	280, 400,500, 550	66, 113,170, 272, 336, 400	24, 48, 96, 120

[a] The feed and permeate have the same velocity and channel configuration.

$$R = \frac{n\sum y_i\hat{y}_i - (\sum y_i)(\sum \hat{y}_i)}{\sqrt{n(\sum y_i^2) - (\sum y_i)^2}\sqrt{n(\sum \hat{y}_i^2) - (\sum \hat{y}_i)^2}} \tag{24}$$

where R is correlation coefficient; $\hat{y}_i$ is the value of the dependent parameter predicted by the model; y is the true value of the dependent parameter; and n is the number of data points. The results by XLSTAT were assumed reliable due to the intensive verification tests conducted against other software packages.

4. Results and discussion

4.1. Dimensionless groups trends based on experimental data

Results from three experimental studies with different DCMD module geometries [29–31], as summarized in Table 3, were used to investigate the trends of the dimensionless groups developed for DCMD in Section 2.2. This was done by calculating the values of four dimensionless numbers; *Sh*, *Nu*, FF, and *Eu*, over a range of *Re* values and for three GF (which correspond to the three geometries of the modules used in the [29–31]. It is important to notice here that the three experimental systems in Table 3 were operated at the same inlet feed and permeate temperatures (60 and 20 °C, respectively), used the same membrane, and were all operated in the laminar flow range.

Fig. 2(a) shows that *Nu* increases with increasing *Re* for all three GF values. This trend is expected because *Nu* is directly proportional to *Re* in convective heat transfer, under both laminar and turbulent flow, due to the significant reduction of flow boundary layer thickness with increasing *Re*. However, the rate of *Nu* change upon changing *Re* is significantly influenced by GF, with the change rate being more

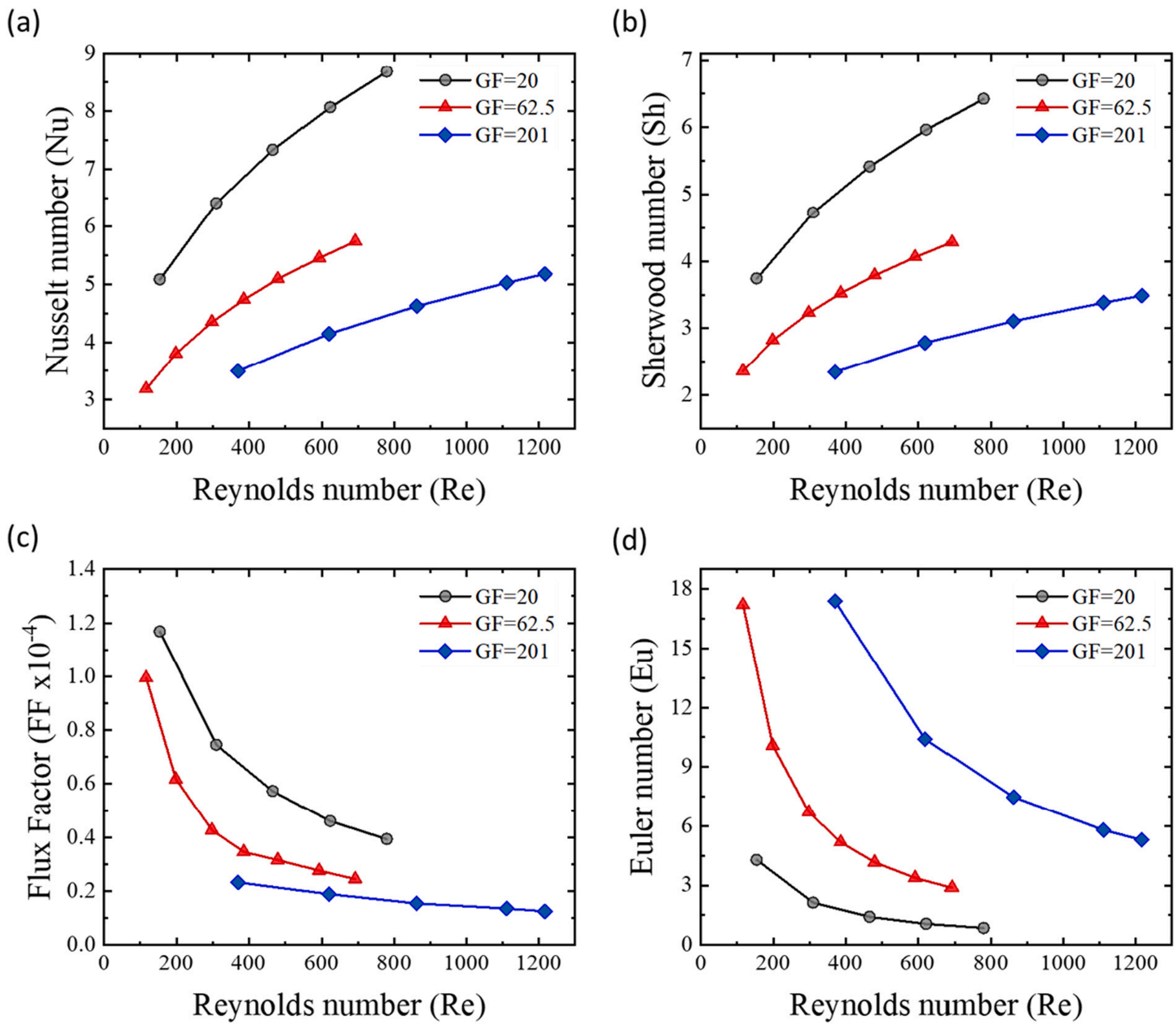

Fig. 2. (a) *Nu* vs. *Re*, (b) *Sh* vs. *Re*, (c) FF vs. *Re*, and (d) *Eu* vs. *Re*, based on parameters obtained from [29–31].

pronounced at lower GF. A bigger GF value can result from either a longer flow channel or a smaller hydraulic diameter, with the former being the most likely reason in full-scale DCMD. Hence, these results indicate that smaller DCMD modules (i.e., ones with low GF) have higher heat transfer coefficients, and therefore higher flux, than full-scale systems, as also reported by [32]. Similar trends are also observed in Fig. 2(b) for *Sh* versus *Re* at different GF values. The increase in *Sh* with *Re* can be explained by the enhanced flow mixing, leading to the suppression of the boundary layer [33]. Similar to *Nu*, *Sh* is also more sensitive to changes in *Re* in smaller systems with low GF. These results indicate that the effectiveness of flow mixing within the feed channel decreases in larger modules with high GF, as also reported by [34].

Fig. 2(c) shows a plot of FF versus *Re* at different GF values, revealing that FF is inversely proportional to GF, which is in line with the aforementioned correlations of *Nu* and *Sh* with GF. However, contrastingly, FF decreases with increasing *Re*. Increasing the feed flow rate increases

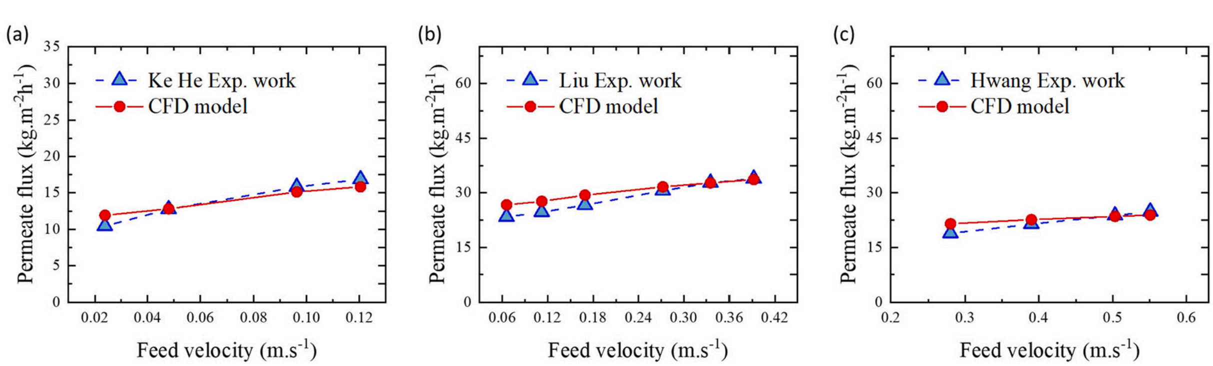

Fig. 3. Validation of our CFD model results using literature-reported experimental DCMD flux data of systems with (a) GF = 20 [31], (b) GF = 62.5 [30], and (c) GF = 201 [29]. Reported experimental uncertainty of experimental data is up to 12%.

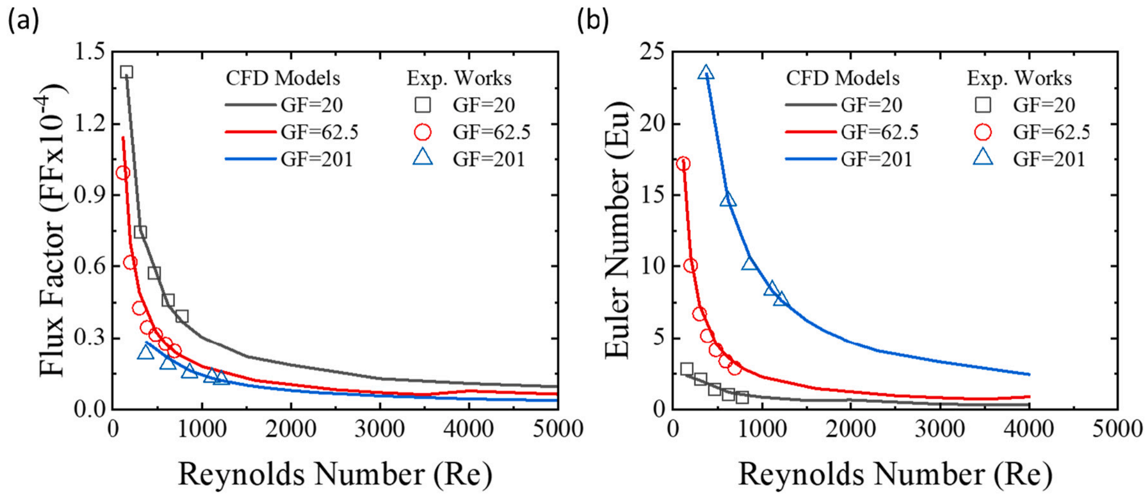

Fig. 4. Experimental and CFD models results for (a) FF vs. *Re* (b) *Eu* vs. *Re*.

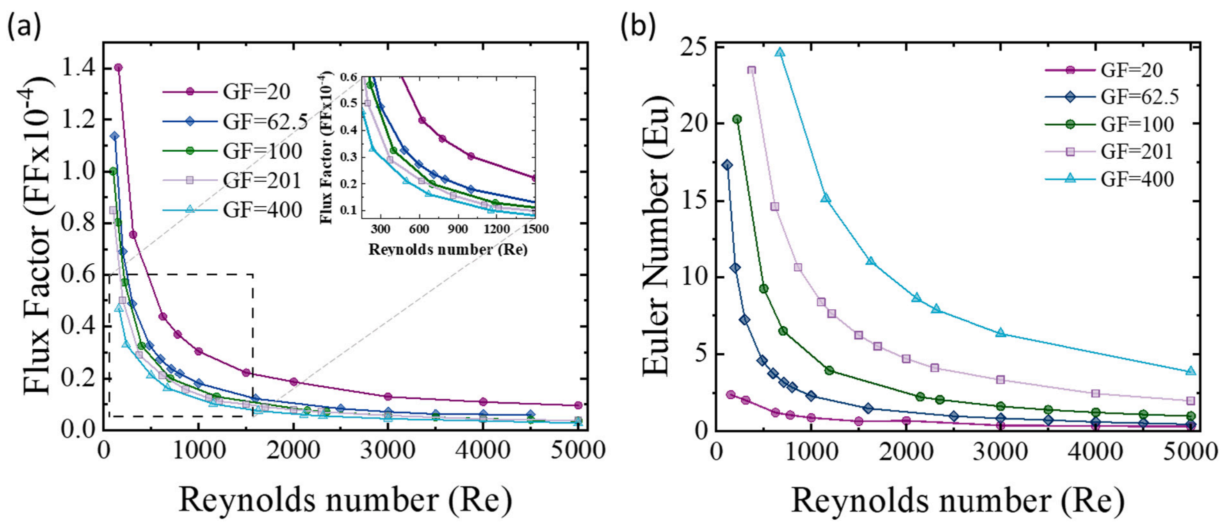

Fig. 5. CFD models result for models with GF of 20, 62.5, 100, 201, and 400 for (a) FF vs. *Re* (b) *Eu* vs. *Re*.

both *Re* and permeate flux. However, the change in the latter gradually reaches a plateau at high *Re* values, at which point the boundary layer resistance becomes negligible and any further increase in velocity has no effect on flux. [35]. Since FF is the ratio of permeate flux to feed flow, the net impact of higher *Re* is a decreasing FF. Fig. 2(d) depicts the change in *Eu* with *Re* for different GF values. *Eu*, and consequently pressure drop within the feed channel (see *Eu* definition in Table 2), is most sensitive to *Re* at high GF and at low *Re* values. As the inverse of the Eu represents the efficiency of converting upstream pressure energy to kinetic energy, this means that the system becomes more efficient at high Re due to the reduced viscous loss through the channel. At Eu = 1, upstream pressure energy provided to the system will equally split into pressure drop and dynamic pressure of the liquid flow, which in turn is converted to flow kinetic energy [36].

Based on the dimensionless groups trends presented in Fig. 2, which were based on data from three different experimental studies, the same trends were observed for all six dimensionless numbers. These trends also conformed to the underlying physical phenomena behind the changes in their values. This lends assurance vis-à-vis the efficacy of these dimensionless groups in describing DCMD systems.

4.2. *Dimensionless groups trends based on CFD results*

Results based on CFD modeling were herein used to extend our assessment of dimensionless groups trends to include turbulent flow regime and to include the feed temperature effect. To gain assurance of the accuracy of our CFD model results, the earlier mentioned experimental DCMD results [29–31], were used to validate our CFD model. In each of the said studies, the inlet velocities for permeate and feed were kept equal and, therefore, this condition was also upheld in our CFD simulations. Fig. 3(a), (b), and (c) display the CFD model's prediction for *J* against feed inlet velocity, along with the corresponding experimental results for modules with GF = 20, 62.5 and, 201 [29–31]. It can be seen that the experimental and CFD flux results match within 3.5%, which was considered to be an excellent match of experimental and modeled data. Fig. 4(a) and (b) display the FF and *Eu* versus *Re* for both the experimental studies [29–31] and CFD models, respectively, where for turbulent flow $k-\omega$ SST turbulence model in STAR CCM+ was implemented. Once again, the experimental and computational results are in excellent agreement.

Fig. 5(a) and (b) demonstrate the CFD results for GF modules of 20, 62.5, 100, 201, and 400. Notice that the *Re* and GF ranges covered in this figure exceed the range of the experimental studies in Table 3 (hence the main purpose of CFD modeling). The two additional scale models (GF =

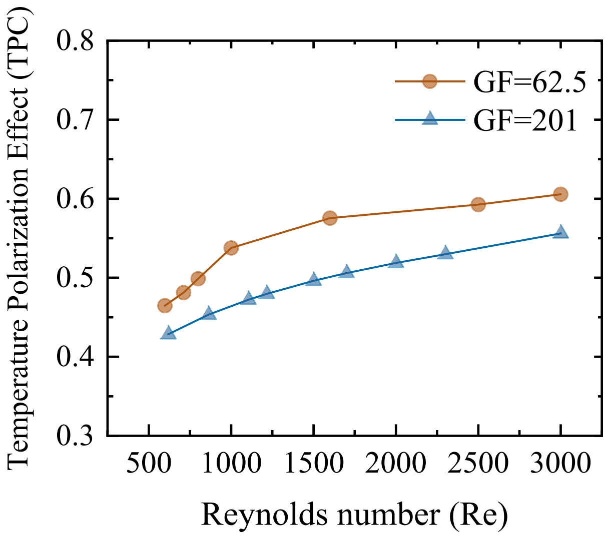

Fig. 6. Temperature polarization coefficient (TPC) vs. *Re* for models with GF = 62.5 and 201.

100 and 400), which were developed utilizing the boundary conditions in [30], fit well within the overall trend of FF and *Eu* under different GF values. Fig. 5(a), which depicts FF versus *Re*, shows that at low *Re*, the GF had a considerable effect on the FF, but this effect decreases as *Re* increases. The FF remains fairly constant within the turbulent range (*Re* > 3000) due to the impact of the viscous sublayer resistance. Therefore, increasing the flow velocity beyond that limit is inconsequential on permeate flux while undesirably increasing the pumping energy. Fig. 5(b) displays the variation of *Eu* with *Re*. The increase in *Eu* with GF implies the possible significant increase in the pressure drop within the system as the module length increases or as its hydraulic diameter decreases. The pressure increases quadratically with feed velocity, while *Eu* was almost constant beyond *Re* > 3000.

To illustrate the effect of the GF on the temperature polarization coefficient (TPC), Fig. 6 shows the TPC values at different *Re* for two modules with GF 62.5 and 201 [29,30]. In both modules, TPC increases with Re while it decreases with GF. This is attributed to the thinning of the thermal boundary layer under turbulent conditions [37]. However, TPC plateaus at *Re* > 3000 due to the effect of the viscous sublayer [38].

To investigate the influence of feed temperature on system performance, FF and *Eu* were calculated based on CFD results at different temperatures for two modules with GF = 201 and 62.5. Fig. 7(a) and (b)

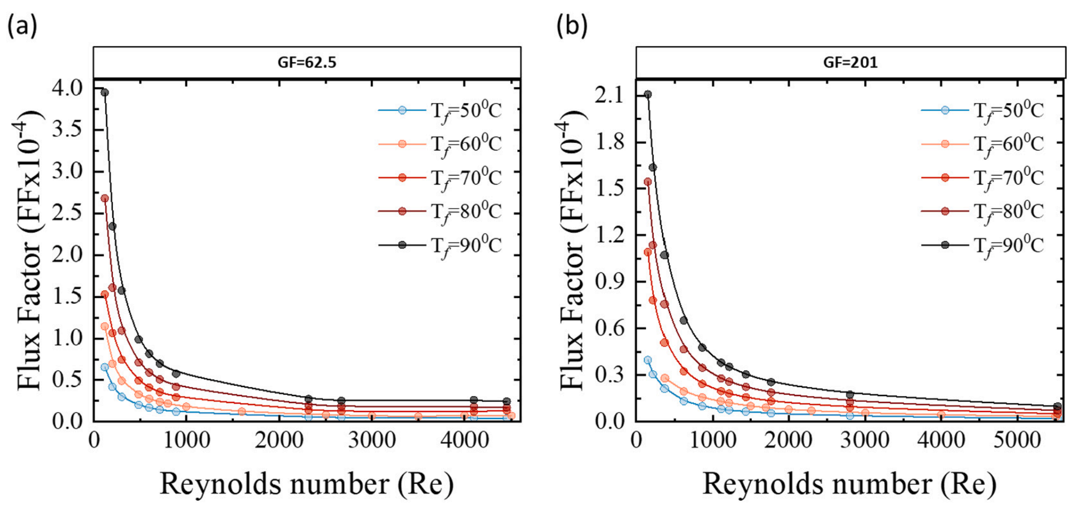

Fig. 7. FF values for (a) module with GF = 62.5, and (b) module with GF = 201, at feed temperature of 50, 60, 70, 80, and 90 °C.

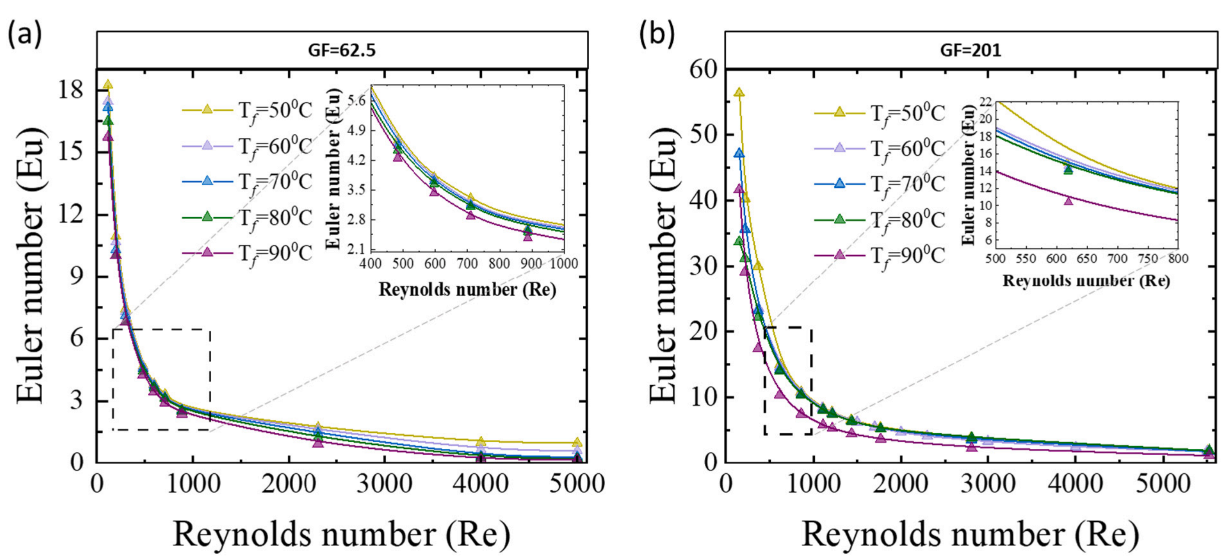

Fig. 8. *Eu* values for (a) module with GF = 62.5, and (b) module with GF = 201, at feed temperature of 50, 60, 70, 80, and 90 °C.

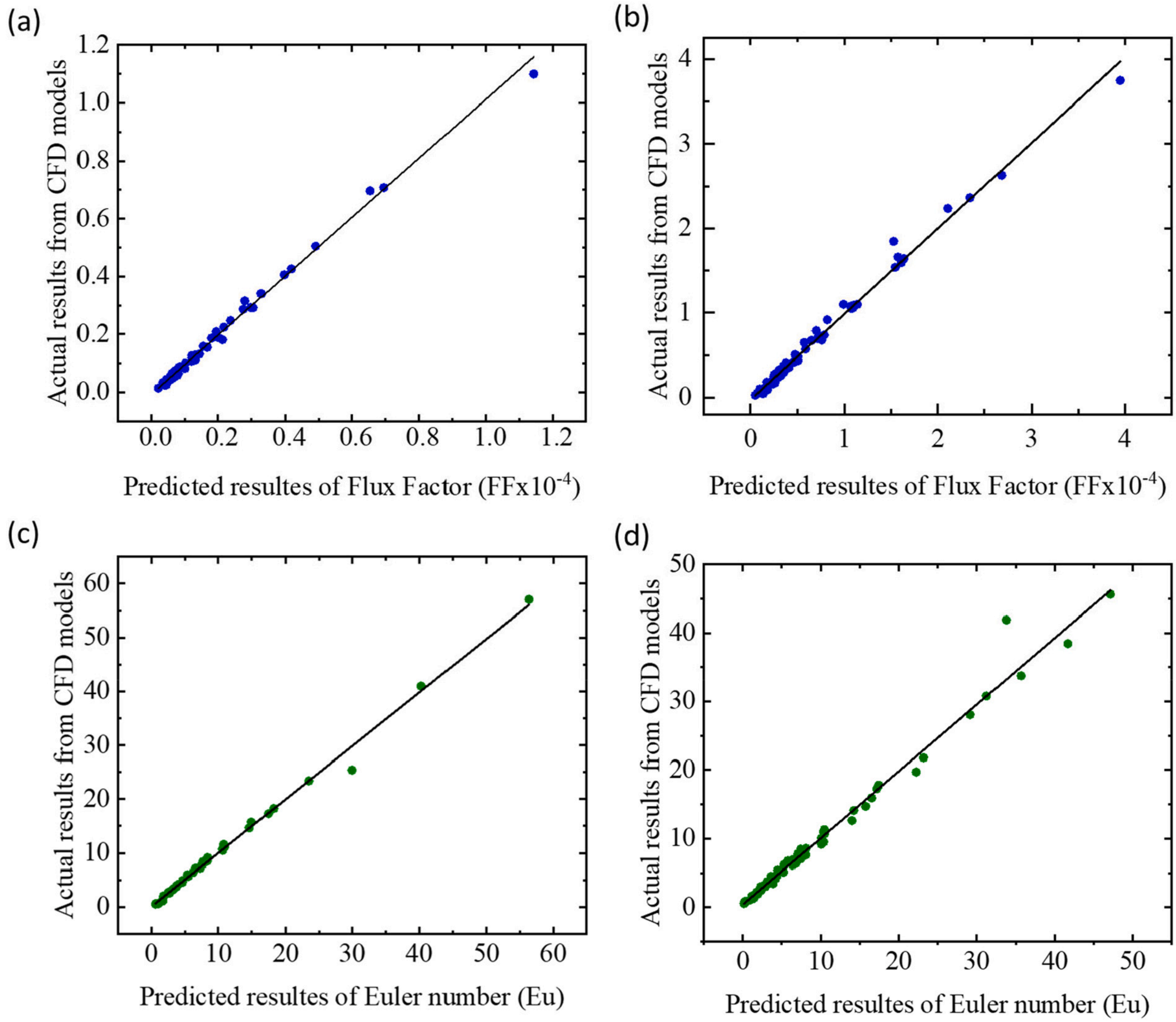

Fig. 9. CFD results vs predicted values from regression equations for (a) Flux Factor at $T < 70^\circ$C, (b) Flux Factor at $T > 70^\circ$C, (c) Euler number at T < 70°C, and (d) Euler number at T > 70°C.

illustrates the results for FF versus *Re* at feed temperatures of 50, 60, 70, 80, and 90 °C for the GF = 201 and 62.5 modules, respectively. FF increases with feed temperature under both GF values, as expected, due to the impact of feed temperature on vapor pressure and, consequently, flux. At any feed temperature, on the other hand, the smaller scale module (GF = 62.5) has about twice the FF compared to the larger scale module (GF = 201). This indicates that flux in larger (i.e., full scale) DCMD systems is always lower than that obtained using their smaller, lab-scale, version. This is in agreement with the observations made in Section 4.1. The corresponding *Eu* results for these two systems are shown in Fig. 8(a) and (b) over the same feed temperatures. Unlike FF, a minor effect of feed temperature on *Eu* was noticed, indicating that the effect of feed temperature on feed channel pressure drop is negligible.

4.3. Development of dimensionless empirical correlations for DCMD

Nonlinear multiple regression analysis was used in this work to create empirical correlations, using the CFD results, for estimating two key dependent DCMD process parameters; flux and pressure drop in the feed channel. The empirical correlations were expressed in terms of dimensionless numbers, to make them useful for DCMD scale up. Two dimensionless groups, FF and *Eu*, were expressed in the correlations as functions of independent dimensionless parameters such as GF, *Re*, and temperature ratio (T*). The latter is defined as the ratio between the feed and permeate temperatures. It is important to mention here that one could attempt to express FF and *Eu* in terms of a range of dimensionless groups from the ones listed in Table 2. However, it is essential to ensure that the dimensionless numbers used do not have interdependencies and that they can describe the system adequately. Since *Sh*, *Sc*, *Nu*, and *Pr* numbers are all dependent on *Re* (as seen, for example, in Fig. 2), we choose to establish a correlation of FF and *Eu* versus *Re*.

Eq. (25) show the best-fit empirical correlation that was achieved for FF as a function of *Re*, GF, and T*, using XLSTAT.

$$FF{\cdot}10^4 = A(Re)^{(b.T^*+c)}(GF)^d \tag{25}$$

where: $T^* = \frac{T_f}{T_p}$, both in Celsius.

And the constants are:

$$\begin{cases} A=156.68, b=0.19, c=-1.4, d=-0.2453, for\, T_f<70^\circ C\, and\, T_p=20^\circ C \\ A=621.68, b=0.15, c=-1.535, d=-0.238, for\, T_f\geq 70^\circ C\, and\, T_p=20^\circ C \end{cases}$$

Eq. (26) shows the best-fit empirical correlation that was achieved for *Eu*:

$$Eu = A(Re)^{(b.T^*+c)}(GF)^d \tag{26}$$

where: $T^* = \frac{T_f}{T_p}$, both in Celsius.

And the constants are:

$$\begin{cases} A = 10.89, b = -2.24\mathrm{E}-0.02, c = -0.8723, d = 1.1943, for\ T_f < 70^\circ C and\ T_p = 20^\circ C \\ A = 13.6, b = -3.4\mathrm{E}-02, c = -0.727, d = 1.0335, for\ T_f \geq 70^\circ C\ and\ T_p = 20^\circ C \end{cases}$$

The equations show an exponential correlation of FF and *Eu* with *Re*, T*, and GF. The coefficient of determination R^2 of the four models is greater than 0.98. It is worth noting that the coefficients (a, b, c, and d) in Eqs. (25) and (26) are different when the feed temperature is below 70 °C than when it is above 70 °C. As discussed earlier, several reports (e.g., [13,39]) indicate that bench/lab scale DCMD tests tend to yield higher fluxes than their bigger versions. This is reflected in the negative exponent of GF (d) in Eq. (25), meaning that GF has a negative effect on permeate flux. The underlying reason is that, with increased module length, the concentration and temperature polarization effects become more pronounced, leading to reduction in permeate flux that is more significant in the larger systems [6]. On the other hand, the exponent of GF in Eq. (26) is positive, due to the increase in pressure drop with GF, meaning that the total pressure loss will be higher in full-scale systems [40].

Finally, Fig. 9(a), (b), (c), and (d) show plots of FF and *Eu* values obtained using the CFD model versus those obtained using Eqs. (25) and (26), under 2 temperature ranges (below and over 70 °C). It is evident that the agreement between the two is excellent, indicating the efficacy of Eqs. (25) and (26) in predicting FF and *Eu*.

5. Conclusions

The performance of a DCMD unit is dependent on a large number of independent and overlapping process variables. Thus, predicting the process performance at increasing scale of operation based on lab-scale experimental results becomes rather difficult. The current work addresses this challenge using dimensional analysis based on the Buckingham Pi-theorem to develop simplified prediction correlations and provide a better understanding of the effects of scaling parameters on the process performance. Based on the dimensional analysis, the MD process was represented by two newly generated dimensionless groups; Flux Factor (FF) and geometry factor (GF), in addition to Euler number (*Eu*), Schmidt number (*Sc*), Reynolds number (*Re*), Nusselt number (*Nu*), and Sherwood number (*Sh*). DCMD CFD models were developed and validated using experimental data to test the new nondimensional relationships at scales that were not previously covered experimentally in literature. The CFD models also help examine the validity of these relationships to predict DCMD prototype performance. The computational and experimental results illustrate that DCMD modules with lower GF have higher values for both *Nu* and *Sh* numbers, which means better heat and mass transfer performance; and thus, results in higher FF. However, the higher GF modules and prototype showed lower values for *Nu*, *Sh*, and FF. These results demonstrate the significant over-prediction of full scale DCMD systems based on lab-scale modules. In addition, DCMD scale is a critical factor that affects the feed channel pressure drop, which has a significant influence on the FF. For GFs of 201 and 62.5, CFD models were run to assess the impact of varying temperature between 50 and 90 °C. The results showed that FF and *Eu* show a direct and inverse relationship, respectively, with feed temperature. The FF and *Eu*, however, show the same trend for the same GF. By including the effects of geometry and feed temperature in non-linear regression analysis, we created and validated two dimensionless equations that can predict the permeate flux and feed pressure loss in DCMD.

CRediT authorship contribution statement

Heba Khafajah is graduate student worked on the model and Pi theorem analysis, Mohamed Ali is associate professor generated the concept, theory, and the model development and supervise Heba. Navya Thomas sharing the analysis and editing work. Professors Isam Janajreh and Hassan Arafat were the co-advisors, the revised the concept and the manuscript. All research team members revised and responded to the reviewers comments.

Declaration of competing interest

The authors declare that they have no known competing financial interests or personal relationships that could have appeared to influence the work reported in this paper.

Acknowledgments

The research reported in this publication was supported by funding from Khalifa University through the Center for Membrane and Advanced Water Technology (CMAT), under grant number RC2-2018-009.

Appendix A. Supplementary data

Supplementary data to this article can be found online at https://doi.org/10.1016/j.desal.2022.115606.

References

[1] A. Hosseinzadeh, J.L. Zhou, A. Altaee, M. Baziar, D. Li, Bioresource technology effective modelling of hydrogen and energy recovery in microbial electrolysis cell by artificial neural network and adaptive network-based fuzzy inference system, Bioresour. Technol. 316 (2020), 123967.
[2] C. Bretas, et al., Comparison of UV, UV/H2O2 and ozonation processes for the treatment of membrane distillation concentrate from surface water treatment: PhACs removal and environmental and human health risk assessment, Chem. Eng. 397 (2020), 125482.
[3] S. Zhao, L. Wardhaugh, J. Zhang, P.H.M. Feron, Condensation, re-evaporation and associated heat transfer in membrane evaporation and sweeping gas membrane distillation, J. Memb. Sci. 475 (2015) 445–454.
[4] R.B. Saffarini, E.K. Summers, H.A. Arafat, J.H. Lienhard V, Economic evaluation of stand-alone solar powered membrane distillation systems, Desalination 299 (2012) 55–62.
[5] S.O. Olatunji, L.M. Camacho, Heat and mass transport in modeling membrane distillation configurations: a review, Front Energy Res. 6 (2018) 130.
[6] L. Francis, N. Ghaffour, A.S. Alsaadi, S.P. Nunes, G.L. Amy, Performance evaluation of the DCMD desalination process under bench scale and large scale module operating conditions, J. Membr. Sci. 455 (2021) 103–112.
[7] A. Ali, C.A. Quist-jensen, F. Macedonio, E. Drioli, Chemical engineering and processing: process intensification optimization of module length for continuous direct contact membrane distillation process, Chem. Eng. Process. 110 (2016) 188–200.
[8] R.de S. Silva, C.D.Á.K. Cavalcanti, R.de C.S.C. Valle, R.A.F. Machado, C. Marangoni, Understanding the effects of operational conditions on the membrane distillation process applied to the recovery of water from textile effluents, Process Saf. Environ. Prot. 145 (2021) 285–292.
[9] M.J. Jamed, A. Alhathal Alanezi, Q.F. Alsalhy, Effects of embedding functionalized multi-walled carbon nanotubes and alumina on the direct contact poly(vinylidene fluoride-co-hexafluoropropylene) membrane distillation performance, Chem. Eng. Commun. 206 (2018) 1035–1057.
[10] M. Rabie, M.F. Elkady, A.H. El-Shazly, Effect of channel height on the overall performance of direct contact membrane distillation, Appl. Therm. Eng. 196 (2021), 117262.
[11] A. Zrelli, B. Chaouchi, S. Gabsi, Impact of the feed concentration on the permeate flux of the solar vacuum membrane distillation equipped with helically coiled fibers, in: IREC 2014 - 5th Int. Renew. Energy Congr, 2016.

[12] R.D. Gustafson, J.R. Murphy, A. Achilli, A stepwise model of direct contact membrane distillation for application to large-scale systems: experimental results and model predictions, Desalination 378 (2016) 14–27.

[13] J. Zhang, S. Gray, J. De Li, Modelling heat and mass transfers in DCMD using compressible membranes, J. Memb. Sci. 387–388 (2012) 7–16.

[14] KKS, L. Song, Pilot-scale studies for direct contact membrane desalination process, Reclamation 134 (2009) 1–122.

[15] D. Winter, Membrane distillation: A thermodynamic, technological and economic analysis, Dissertation. doi:10.2370/9783844037067.

[16] I. Hitsov, et al., Calibration and analysis of a direct contact membrane distillation model using Monte Carlo filtering, J. Membr. Sci. 515 (2017) 63–78.

[17] I. Hitsov, L. Eykens, W. De Schepper, K. De Sitter, C. Dotremont, I. Nopens, Full-scale direct contact membrane distillation (DCMD) model including membrane compaction effects, J. Membr. Sci. 524 (2017) 245–256.

[18] G. Dong, J.F. Kim, J.H. Kim, E. Drioli, Y.M. Lee, Open-source predictive simulators for scale-up of direct contact membrane distillation modules for seawater desalination, Desalination 402 (2017) 72–87.

[19] L. Rend, M. Ram, C. Ocampo-l, Applied sciences mathematical model for scaling up bioprocesses using experiment design combined with Buckingham pi theorem, Appl. Sci. 11 (2021) 11338.

[20] M.F. Islam, L.M. Lye, Combined use of dimensional analysis and modern experimental design methodologies in hydrodynamics experiments, Ocean Eng. 36 (2009) 237–247.

[21] R.R. Patel, D.S. Thompson, G.A. Riveros, W.D. Hodo, J.F. Peters, F.J. Acosta, ScienceDirect dimensional analysis of structural response in complex biological structures, Math. Comput. Simul. 172 (2020) 305–320.

[22] F. Salmani, M.R. Mahpeykar, E.A. Rad, Estimating heat release due to a phase change of high-pressure condensing steam using the Buckingham pi theorem, Eur. Phys. J. Plus 134 (2018) 48.

[23] A. Najib, J. Orfi, H. Alansary, E. Ali, Application of the Buckingham $\prod$ theorem to model the multiple effect vacuum membrane distillation, J. Therm. Sci. Eng. Appl. 14 (2021), 031003-1.

[24] P. Yazgan-Birgi, M.I. Hassan Ali, H.A. Arafat, Comparative performance assessment of flat sheet and hollow fiber DCMD processes using CFD modeling, Sep. Purif. Technol. 212 (2019) 709–722.

[25] Ó. Andrjesdóttir, et al., An experimentally optimized model for heat and mass transfer in direct contact membrane distillation, Int. J. Heat Mass Transf. 66 (2013) 855–867.

[26] L.M. Camacho, et al., Advances in membrane distillation for water desalination and purification applications, Water (Switzerland) 5 (2013) 94–196.

[27] M.M. Ghaleni, A.Al Balushi, M. Bavarian, S. Nejati, in: Modeling and Design of a Solar-Assisted High-Performance Direct Contact Membrane Distillation System. Computer Aided Chemical Engineering 44, 2018, pp. 1921–1926.

[28] B. Zohuri, Dimensional Analysis Beyond the Pi Theorem, 2017, https://doi.org/10.1007/978-3-319-45726-0.

[29] C. Liu, Y. Chen, W. Sheu, C. Wang, Effect of flow deflector on the flux improvement in direct contact membrane distillation, Desalination 253 (2010) 16–21.

[30] H.J. Hwang, K. He, S. Gray, J. Zhang, I.S. Moon, Direct contact membrane distillation (DCMD): experimental study on the commercial PTFE membrane and modeling, J. Membr. Sci. 371 (2011) 90–98.

[31] K. He, H.J. Hwang, M.W. Woo, I.S. Moon, Production of drinking water from saline water by direct contact membrane distillation (DCMD), J. Ind. Eng. Chem. 17 (2011) 41–48.

[32] M. Khoshvaght-Aliabadi, Influence of different design parameters and Al2O3-water nanofluid flow on heat transfer and flow characteristics of sinusoidal-corrugated channels, Energy Convers. Manag. 88 (2014) 96–105.

[33] D. Sebastia-Saez, S. Gu, P. Ranganathan, Volume of fluid modeling of the reactive mass transfer of CO2 into aqueous amine solutions in structured packed elements at microscale, Energy Procedia 63 (2014) 1229–1242.

[34] G. Huo, X. Guo, Numerical analyses of heterogeneous clc reaction and transport processes in large oxygen carrier particles, Processes 9 (2021) 1–21.

[35] M. Gryta, Effectiveness of water desalination by membrane distillation process, Membranes (Basel) 2 (2012) 415–429.

[36] Y.S. Rane, J.O. Marston, Computational study of fluid flow in tapered orifices for needle-free injectors, J. Control. Release 319 (2020) 382–396.

[37] Z. Kuang, R. Long, Z. Liu, W. Liu, Analysis of temperature and concentration polarizations for performance improvement in direct contact membrane distillation, Int. J. Heat Mass Transf. 145 (2019), 118724.

[38] S. Soukane, M.W. Naceur, L. Francis, A. Alsaadi, N. Ghaffour, Effect of feed flow pattern on the distribution of permeate fluxes in desalination by direct contact membrane distillation, Desalination 418 (2017) 43–59.

[39] L. Eykens, I. Hitsov, K. De Sitter, C. Dotremont, L. Pinoy, B. Van Der Bruggen, Direct contact and air gap membrane distillation: differences and similarities between lab and pilot scale, Desalination 422 (2017) 91–100.

[40] T.Y. Cath, V.D. Adams, A.E. Childress, Experimental study of desalination using direct contact membrane distillation: a new approach to flux enhancement, J. Membr. Sci. 228 (2004) 5–16.